



# Light propagation properties of the $\text{Bi}_2\text{ZnOB}_2\text{O}_6$ acentric biaxial crystal: angular orbital momentum from conical diffraction

Alain Brenier, Andrzej Majchrowski, Edward Michalski

## ► To cite this version:

Alain Brenier, Andrzej Majchrowski, Edward Michalski. Light propagation properties of the  $\text{Bi}_2\text{ZnOB}_2\text{O}_6$  acentric biaxial crystal: angular orbital momentum from conical diffraction. *Optical Materials*, 2019, 91, pp.286 - 291. 10.1016/j.optmat.2019.03.035 . hal-02461595

**HAL Id: hal-02461595**

**<https://hal.science/hal-02461595>**

Submitted on 30 Jan 2020

**HAL** is a multi-disciplinary open access archive for the deposit and dissemination of scientific research documents, whether they are published or not. The documents may come from teaching and research institutions in France or abroad, or from public or private research centers.

L'archive ouverte pluridisciplinaire **HAL**, est destinée au dépôt et à la diffusion de documents scientifiques de niveau recherche, publiés ou non, émanant des établissements d'enseignement et de recherche français ou étrangers, des laboratoires publics ou privés.

## **Light propagation properties of the $\text{Bi}_2\text{ZnOB}_2\text{O}_6$ acentric biaxial crystal: angular orbital momentum from conical diffraction**

Alain Brenier<sup>1</sup>, Andrzej Majchrowski<sup>2</sup>, Edward Michalski<sup>3</sup>

<sup>1</sup>Univ Lyon, Université Claude Bernard Lyon 1, CNRS, Institut Lumière Matière, F-69622, LYON, France

<sup>2</sup>Institute of Applied Physics, Military University of Technology, 2 Gen. W. Urbanowicza Str., 00-908 Warsaw, Poland.

<sup>3</sup>Institute of Optoelectronics, Military University of Technology, 2 Gen. W. Urbanowicza Str., 00-908 Warsaw, Poland.

*Abstract : We have studied a slab of an acentric biaxial  $\text{Bi}_2\text{ZnOB}_2\text{O}_6$  single crystal grown by the Kyropoulos method under conditions of low temperature gradients, oriented perpendicular to the optical axis. We focused slightly behind the sample the Gaussian beam from a He-Ne laser at 632.8 nm and we made magnified images of the near field intensity on a CCD camera. A reference beam was taken from the entrance and redirected on the CCD screen to obtain a controlled wedge fringe pattern visualising the phase of the wave. The specific rotatory power was measured to be 2.74 rad/cm. We present results of conoscopy patterns obtained launching through the crystal slab a left-circular polarized beam and projecting the output beam on a right-circular polarization state or on a linearly polarization state at  $-45^\circ$  from the horizontal axis. All the experimental results (optical activity, intensity and phase of the output wave and vortices) are well described by a theoretical model based on the bi-anisotropy of the BZBO crystal. The orbital angular momentum is calculated to be  $0.996 \hbar/\text{photon}$  for the output circular projection and  $0.456 \hbar/\text{photon}$  for the linear projection.*

## 1. Introduction

The acentric biaxial  $\text{Bi}_2\text{ZnOB}_2\text{O}_6$  (BZBO) oxy-borate crystal can be elaborated in bulk size by top-seeded Kyropoulos growth method [1, 2]. It is non-hygroscopic and stable in a moist environment. Neodymium doping is also possible with high crystal quality [3]. Infra-red spectroscopy, transmittance and refractive indices measurements have been done. It was found that phase matching exists for second harmonic generation of the 1064 nm YAG:Nd laser radiation and its nonlinear optical coefficients have been determined by the Marker fringes method. So up to now this crystal received attention because it belongs to the well-known family of the acentric borate crystals endowed with quadratic nonlinearities and promising optical properties: high transparency in the UV domain and a high optical damage threshold. They are ideal for responding to the need of high power UV and visible all-solid state light sources, up to the fifth harmonic generation (213 nm) of the 1064 nm YAG:Nd fundamental wavelength in some cases. Their optical properties depend on borate anionic groups in a comprehensive modelling [4-6].

On the other hand biaxial crystals, acentric or not, have an interesting property of linear optics: they can transfer an orbital angular momentum (OAM) to light propagating in directions close to the crystal optical axis. The OAM of an optical beam is the effect of the linear momentum acting off-axis with respect to its centre [7]. Helical phase-front beams, for example Laguerre-Gaussian modes, have such  $l \hbar/\text{photon}$  OAM related to their  $\exp(-il\varphi)$  transverse phase variation. This momentum is due to the wave structure and can be in addition to the spin angular momentum (SAM) which is due to the polarization. Several devices can be used to generate beams with OAM. Let us cite the insertion in the beam path of a phase-plate with a thickness increasing with the azimuthal angle [8] or a spatial light modulator based on liquid crystals whose refractive index is modified by an electric field [9]. Insertion of cylindrical lenses is another route [10].

Going back to biaxial crystals, the propagation along the optical axis of a focused beam leads to its conical refraction (CR, instead of the usual double-refraction) and so its emergence as a hollow cylinder [11-13]. Nowadays applications of CR have been found, let us only cite the optical trapping of light [14]. The key-point for the present work is that the beam emerges also with modified OAM and SAM as it was calculated by Berry [15]. Theoretical predictions were nicely experimentally verified in the case of the centro-symmetric  $\text{KGd}(\text{WO}_2)_4$  crystals [16].

This work is devoted to the biaxial BZBO crystal. Because it is acentric, the light propagation is modified by the optical activity (this is a Pasteur medium) as we will show. We experimentally exhibit the CR of a laser beam in the near and far fields, and we study the intensity and the phase of the emergent waves. The connection with the OAM and SAM is obtained through a theoretical model of wave propagation including the birefringence, the optical activity and more generally the crystal bi-anisotropy.

## 2. Light propagation through a bi-anisotropic material

### 2.1 Far field pattern

Let us first find the plane wave eigen-modes propagating through a bi-anisotropic material. Their complex electric field is written as  $\mathbf{E}(\mathbf{r})\exp(\mathbf{k}'_t \cdot \mathbf{r})$  with a similar writing for  $\mathbf{H}$ ,  $\mathbf{B}$  and  $\mathbf{D}$  fields and where  $\mathbf{k}'_t$  has the meaning of the refracted (and transmitted) wave-vector inside the material. We can choose a transverse frame  $x_1, x_2, x_3$  whose third axis  $x_3$  is parallel to  $\mathbf{k}'_t(r, \varphi)$ ,  $(r, \varphi)$  being the polar and azimuthal angles defined from the  $x', y', z'$  frame in Fig. 1 ( $z'$  is the optical axis of the biaxial crystal). More details can be found in ref. [17]. Inserting these field expressions inside Maxwell-Ampère and Maxwell-Faraday equations, we find the following relations between the components:

$$\begin{bmatrix} E_1 \\ E_2 \end{bmatrix} = \frac{\omega}{k'_t} \begin{bmatrix} 0 & 1 \\ -1 & 0 \end{bmatrix} \begin{bmatrix} B_1 \\ B_2 \end{bmatrix} \quad (1)$$

$$\begin{bmatrix} H_1 \\ H_2 \end{bmatrix} = -\frac{\omega}{k'_t} \begin{bmatrix} 0 & 1 \\ -1 & 0 \end{bmatrix} \begin{bmatrix} D_1 \\ D_2 \end{bmatrix} \quad (2)$$

On the other hand, the constitutive relations of a bi-anisotropic material [18-19] in the  $\mathbf{DB}$  representation are:

$$\mathbf{E} = \boldsymbol{\kappa} \cdot \mathbf{D} + \boldsymbol{\chi} \cdot \mathbf{B} \quad (3)$$

$$\mathbf{H} = \boldsymbol{\gamma} \cdot \mathbf{D} + \boldsymbol{\nu} \cdot \mathbf{B} \quad (4)$$

At this step the  $\boldsymbol{\kappa}$ ,  $\boldsymbol{\chi}$ ,  $\boldsymbol{\gamma}$  and  $\boldsymbol{\nu}$  are 3-D tensors with components written in any frame. Then the components in Eq. (3) and (4) can be transformed towards the  $(x_1, x_2, x_3)$  transverse frame

(with an underlined notation) from their expression known in the dielectric xyz frame. For example the inverse permittivity tensor is expressed as  $\underline{\mathbf{\kappa}}$ :

$$\underline{\mathbf{\kappa}}(r, \varphi) = S_2(r, \varphi)(S_1 \mathbf{\kappa} S_1^{-1}) S_2^{-1}(r, \varphi) \quad (5)$$

where  $S_1$  is the 3-D rotation making the  $(x, y, z) \rightarrow (x', y', z')$  frame transfer and  $S_2(r, \varphi)$  makes the  $(x', y', z') \rightarrow (x_1, x_2, x_3)$  transfer. The **DB** representation is very convenient because the **D** and **B** fields are transverse so  $D_3=B_3=0$  and Eq. (3) and (4) simplify as:

$$\begin{bmatrix} E_1 \\ E_2 \end{bmatrix} = [\underline{\mathbf{\kappa}}]_{2 \times 2} \begin{bmatrix} D_1 \\ D_2 \end{bmatrix} + [\underline{\mathbf{\chi}}]_{2 \times 2} \begin{bmatrix} B_1 \\ B_2 \end{bmatrix} \quad (6)$$

$$\begin{bmatrix} H_1 \\ H_2 \end{bmatrix} = [\underline{\mathbf{\gamma}}]_{2 \times 2} \begin{bmatrix} D_1 \\ D_2 \end{bmatrix} + [\underline{\mathbf{v}}]_{2 \times 2} \begin{bmatrix} B_1 \\ B_2 \end{bmatrix} \quad (7)$$

where 2X2 means the 2-D restriction of the tensors to the 1 and 2 transverse coordinates.

We can determine the four transverse fields of each eigen-mode by combining the four (1), (2), (6) and (7) equations. With Eq. (2) introduced inside Eq. (7) we obtain:

$$\begin{bmatrix} B_1 \\ B_2 \end{bmatrix} = [\underline{\mathbf{v}}]_{2 \times 2}^{-1} \left\{ -[\underline{\mathbf{\gamma}}]_{2 \times 2} + \frac{\omega}{\kappa'_t} \begin{bmatrix} 0 & -1 \\ 1 & 0 \end{bmatrix} \right\} \begin{bmatrix} D_1 \\ D_2 \end{bmatrix} \quad (8)$$

Then with Eq. (1), (6) and (8) we find the **D** eigen-modes as the non-vanishing solutions of:

$$\left\{ [\underline{\mathbf{\kappa}}]_{2 \times 2} - \mu_0 [\underline{\mathbf{\chi}}]_{2 \times 2} [\underline{\mathbf{\gamma}}]_{2 \times 2} + \mu_0 \frac{\omega}{\kappa'_t} \left\{ [\underline{\mathbf{\chi}}]_{2 \times 2} \begin{bmatrix} 0 & -1 \\ 1 & 0 \end{bmatrix} - \begin{bmatrix} 0 & -1 \\ 1 & 0 \end{bmatrix} [\underline{\mathbf{\gamma}}]_{2 \times 2} \right\} - \mu_0 \left( \frac{\omega}{\kappa'_t} \right)^2 \begin{bmatrix} 1 & 0 \\ 0 & 1 \end{bmatrix} \right\} \begin{bmatrix} D_1 \\ D_2 \end{bmatrix} = \begin{bmatrix} 0 \\ 0 \end{bmatrix} \quad (9)$$

where we have restricted to the case useful in the present work of an isotropic and non-magnetic permeability  $\mathbf{v} = 1/\mu_0$ .

Equating to zero the determinant leads to the generalisation of the well-known Fresnel equation which is a fourth degree equation including odd (1 and 3) degrees. Its two solutions in a given propagation direction are the eigen-values  $\frac{\omega}{\kappa'_{t\pm}}$  leading to the two  $\begin{bmatrix} D_1 \\ D_2 \end{bmatrix}_{\pm}$  eigen-

modes. The eigen-modes of the other fields and specially the electric field are obtained from Eq. (1), (2) and (8).

The electric field  $\mathbf{E}$  of the input beam at the entrance face of the crystal is a priori known in the  $(x', y', z')$  frame. This field can be decomposed in plane waves from its 2D-Fourier transform  $\hat{\mathbf{E}}$ . Each plane wave propagates inside the crystal after refraction according to a calculation detailed in Ref. [17] and summarized as:

-First step: we obtain the  $\hat{\mathbf{E}}$  components in the  $(\mathbf{x}_1, \mathbf{x}_2, \mathbf{x}_3)$  transverse frame

-Second step: with the help of the eigen-modes we obtain the  $\hat{\mathbf{E}}$  tangential components at the output crystal face after a path  $L$ .

-Third step: we go back to the  $(x', y', z')$  frame which leads to the  $[\hat{\mathbf{E}}(L, k_{ix'}, k_{iy'})]_{x'y'}$  electric far field pattern.

## 2.2 Near field pattern after the material

After propagation in air over a distance  $d$  behind the crystal, all the plane waves constituting the far field interfere, in other words the electric near field is obtained as an inverse 2D-Fourier transform  $[\mathbf{E}(x', y', d)]_{x'y'} = iFT \left\{ \exp(ik_{iz'}d) [\hat{\mathbf{E}}(L, k_{ix'}, k_{iy'})]_{x'y'} \right\}$ . From discretisation the inverse Fourier transform is calculated with the inverse Fast Fourier Transform (iFFT) algorithm of the Matlab package.

## 2.3 OAM and SAM after the material

In the paraxial approximation used here for calculating the light propagation in air after the conical diffraction inside the crystal, the beam OAM component along the propagation direction involves only the transverse electric field. The OAM/photon is obtained by the expression [15]:

$$J_{orb} = \frac{\hbar \text{Im} \iint d\mathbf{R} (\mathbf{E}^* \cdot \partial_\varphi \mathbf{E})}{\iint d\mathbf{R} (\mathbf{E}^* \cdot \mathbf{E})} \quad (10)$$

while the SAM/photon is given by:

$$J_{sp} = \frac{\hbar \text{Im} \iint d\mathbf{R} (e_z \cdot \mathbf{E}^* \times \mathbf{E})}{\iint d\mathbf{R} (\mathbf{E}^* \cdot \mathbf{E})} \quad (11)$$

These formulas show that the OAM depends on the angular variation  $\varphi$  of the electric field around the centre of the beam and that the SAM depends on the polarization.

## 3. Experimental set-up for CR and OAM visualization

BZBO single crystals were grown from stoichiometric melts by means of Kyropoulos technique on [001] oriented seeds. Detailed description of BZBO crystallization and morphology of as-grown single crystals can be found in our previous paper [3].

The beam from a 632.8 nm Helium-Neon laser, focused into a 16  $\mu\text{m}$  waist spot behind the BZBO sample (1 cm) with a 5 cm focal length lens L1, is schematically represented in Fig. 1. The intensity of the near field (red circle) resulting of conical diffraction behind the crystal is imaged through the L2 lens (10 cm focal length) with a magnification 15 on the ocean Optics CCD screen, the magnification being calculated from the lens-camera distance. The far field is obtained in a separate measurement replacing L2 by a L3 lens (20 cm focal length and not shown in the figure), the CCD screen being located in the L3 focal plane. All the lenses are achromatic doublets from Thorlabs. In Fig. 1 we can see that a linear polarizer and an achromatic quarter-wave plate (from Thorlabs) can be introduced in the beam path before the sample in order to make the beam polarized linearly, circularly or elliptically. After the sample similar optical components are used to analyse the beam and decompose it in different polarization states.

In order to visualise the phase of the near field, a reference beam is taken from the input beam with a 50/50 beam splitter, is expanded by a telescope and redirected towards the CCD screen by a second 50/50 beam splitter. The whole set-up is similar to a Mach-Zehnder interferometer and the two beams go through the same output linear polarizer Pol2 allowing the interference. On the output beam-splitter face the two beams are a few mm separated (horizontally, vertically or in any other direction) in order to create a controlled wedge fringe pattern with the desired resolution.

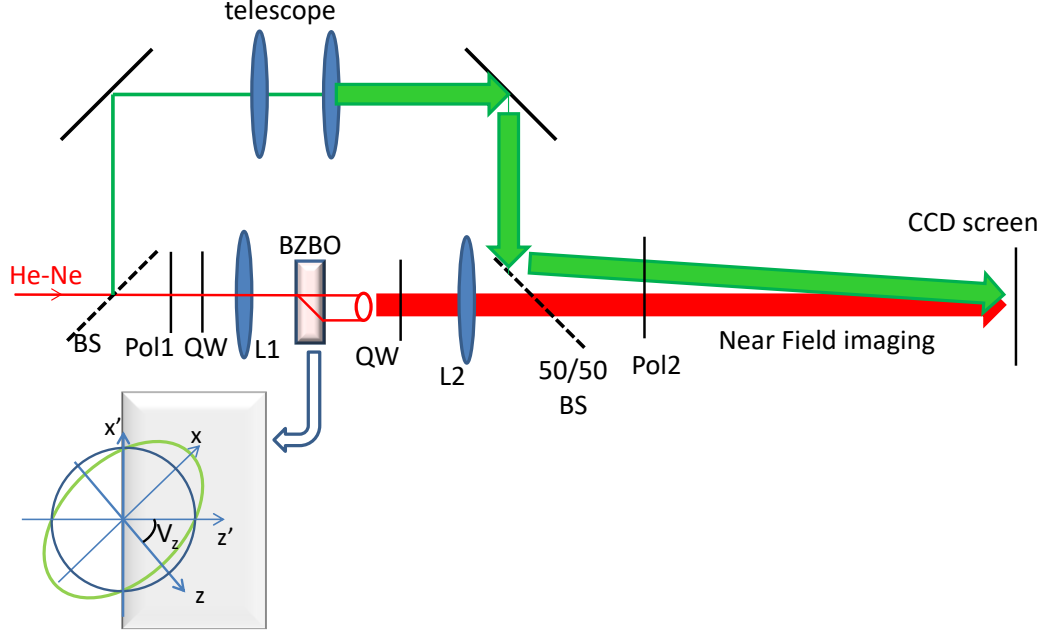


Fig. 1 Experimental set-up for CR and OAM visualisation.

## 4. Results and interpretation

### 4.1 Characterisation of the optical activity of the $\text{Bi}_2\text{ZnOB}_2\text{O}_6$ acentric crystal

The BZBO crystal is orthorhombic with point group  $mm2$  ( $C_{2v}$ ). The  $x$ ,  $y$ ,  $z$  axes of the dielectric frame coincide respectively with the  $b$ ,  $c$ ,  $a$  crystallographic axes. So the optical axis of the transparent crystal lies in the  $xz=ba$  plane with the  $V_z$  angle with the  $z$  axis close to  $42.6^\circ$ , depending slightly on the wavelength. The inverse permittivity tensor  $\boldsymbol{\kappa}$  is diagonal in the  $xyz$  frame and its components are real (we limit this work to the domain of transparency of the material) and obtained through the measured three principal refractive indices [2]:  $n_1=2.0679$ ,  $n_2=2.105$ ,  $n_3=2.1541$ .

The  $\boldsymbol{\chi}$  and  $\boldsymbol{\gamma}$  tensors are constituted of a symmetric and an antisymmetric part. However in the present work our goal is to describe the optical activity as we show in the following of this sub-section. In this case only the antisymmetric part is necessary:

$$\boldsymbol{\chi} = \boldsymbol{\chi}_a \quad (12)$$

$$\boldsymbol{\gamma} = -\boldsymbol{\chi}_a^T \quad (13)$$

where the upper-script  $T$  means the matrix transpose. In this case the generalized Fresnel equation is biquadratic (no odd degrees). In the  $mm2$  BZBO symmetry there are only two independent parameters, real in the domain of transparency:



$$\chi_a = i \begin{bmatrix} 0 & 0 & \chi_{axz} \\ 0 & 0 & 0 \\ \chi_{azx} & 0 & 0 \end{bmatrix} \quad (14)$$

where the tensor components are written in the xyz dielectric frame. The two  $\chi_{axz}$  and  $\chi_{azx}$  can be investigated as follow.

In this sub-section, removing the two quarter-wave plates in the experimental set-up we can launch a beam with a vertical polarization and detect it on the CCD with a horizontal analyser. As a preliminary step the BZBO sample is replaced by a centro-symmetric crystal with the same orientation ( $z'$ ) of its optical axis, let us say KGd(WO<sub>2</sub>)<sub>4</sub> (KGW). The result of the far field intensity is shown in Fig. 2 (a1) (experimental) and (a2) (theoretical). We can see that the centre is extinguished because it corresponds to propagation through an isotropic direction between two crossed polarizers.

To the contrary the similar experiment conducted with the BZBO sample leads to a brilliant centre in Fig. 2 (a3). The reason is that the initial polarization has been rotated by an angle measured to be 100° (it is easily measured by searching with the output polarizer the angle giving the light extinction). The specific rotatory power  $\rho$  (rad/cm) is due to the fact that the two eigen-modes are left and right circularly polarized with a difference  $\Delta k$  in their wavenumbers:

$$\rho = \Delta k / 2 \quad (15)$$

We measured 100° rotation for 0.6375 cm sample thickness, so  $\rho = 2.74$  rad/cm. Because  $\Delta k$  is related to the discriminant of Fresnel equation we find the relation:

$$\underline{\chi}_{a11} + \underline{\chi}_{a22} = \frac{\lambda_c}{\pi n_y^2} \rho \quad (16)$$

The two independent parameters in Eq. (14) cannot be determined separately from this experiment, only their sum is determined:

$$\chi_{axz} + \chi_{azx} = - \frac{\underline{\chi}_{a11} + \underline{\chi}_{a22}}{\cos(V_z) \sin(V_z)} \quad (17)$$

In the present work we will not conduct more refined experiments to determine separately these two parameters, but we will show that using as a try the same value for both of them half the value from Eq. (17), we obtain a satisfactory description of all the experimental figures. The theoretical Fig. 2 (a4) can be compared to Fig. 2 (a3).

The optical activity has also a noticeable influence in the phase of the wave despite that in this sub-section the input and output beams have no OAM. The intensity of the near field in the focal plane is represented in Fig. 2 (b1) (experimental) and 2 (b2) (theoretical) in the case of the centro-symmetric KGW. The intensity vanishes in the horizontal  $xz$ -plane which constitutes a border such that the phase of the wave above and below have an abrupt  $\pi$  rad difference as it is shown in Fig. 2 (c1) (experimental) and 2 (c2) theoretical) following the brilliant fringes. To the contrary in the BZBO case, the optical activity not only modifies the field intensity (Fig. 2 (b3) and (b4)) but also the phase: we can see following through the horizontal  $xz$ -plane the brilliant fringes in Fig. 2 (c3) and (c4) that they are no more head to foot with the dark fringes: the phase variation is smoothed.

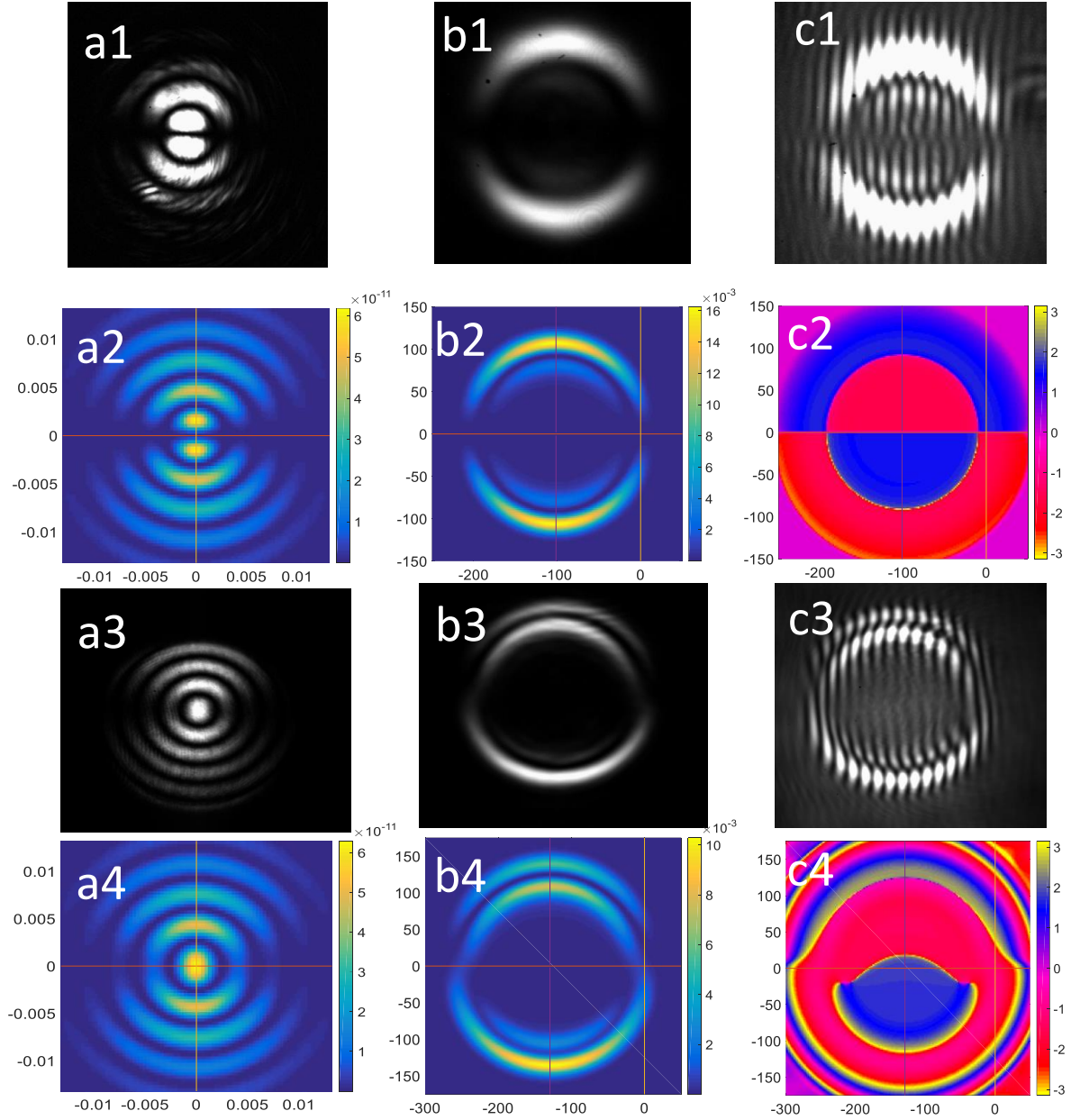


Fig. 2 See text in subsection 4.1. Column a: intensity of the far field; column b: intensity of the near field in the focal plane; column c: 1 and 3: interference with the reference beam, 2 and 4: phase in the focal plane (vertical scale in rad.). Lines 1 and 3: experimental, lines 2 and 4: theoretical.

#### 4.2 Configuration generating an angular orbital momentum close to integer

In this sub-section, thanks to a QW plate and a vertical polarizer in the experimental set-up we launch a beam through the BZBO sample with a left-circular polarization with the goal to

project the output beam on a right-circular state. For that purpose we detect the output beam on the CCD through a right-circular polarizer constituted with a second QW with its fast axis perpendicular to the one of the input QW plate, followed by a horizontal analyser and finally followed by a third QW plate. However the third QW plate is not actually installed because it will change neither the intensity nor the phase of the output wave and it should prevent the interference with the reference wave.

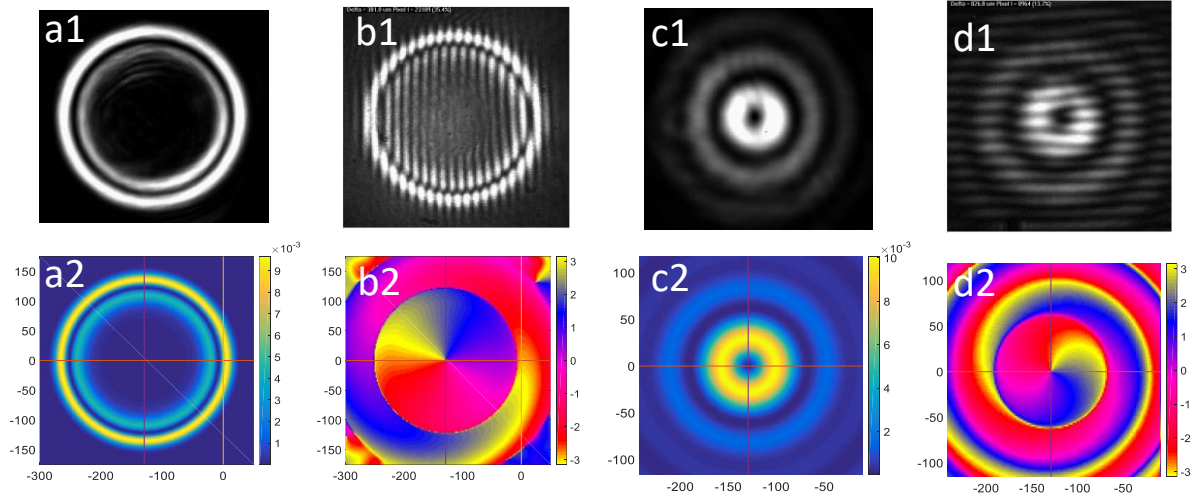


Fig. 3 See text in subsection 4.2. Columns a and b: focal plane, columns c and d: Raman spot plane. Columns a and c: near field intensity; column b and d: 1: interference with the reference beam and phase (vertical scale in rad.). Line 1: experimental, lines 2: theoretical.

In the focal plane we observe mainly two brilliant rings separated by a dark one (Fig. 3 (a1) experimental) whose diameter is  $240\ \mu\text{m}$ , that is to say much higher than the beam diameter ( $32\ \mu\text{m}$ ). The experimental diameter is very close to the calculated one (Fig. 3 (a2)). The interference pattern with the reference beam is shown in Fig. 3 (b1). We can see the modulation of the two brilliant rings by the alternation of dark and brilliant fringes. The key-point is that there are 19 brilliant fringes in the upper external semi-circle and 20 in the lower one. Similarly there is one brilliant fringe more in the lower semi-circle of the internal ring. The meaning of the surplus fringe is that the right circular output wave includes a  $2\pi$  phase variation in addition to the phase of the reference wave and an inspection of the two optical paths of the waves (Fig. 1) allows to determine that this phase variation is incremental if we perform an anti-clock wise rotation around the centre of the circles. These experimental observations are in full agreement with the phase of the right circular output wave calculated

by the model of section 2 and represented in Fig. 3 (b2). More, the OAM calculated with Eq. (10) is found to be  $0.996 \hbar/\text{photon}$  and the SAM is  $-1 \hbar/\text{photon}$ . Let us add that the dark ring is a boundary on which the phase is not defined (Fig. 3 (b2)). It separates the field in two domains with a  $\pi$  rad phase difference visualised by head to foot brilliant and dark fringes in Fig. 3 (b1). Fig. 3 (b2) exhibits also an optical vortex in its centre where the phase is not defined.

In the plane about 2 cm further (the Raman spot plane) the left-circular polarized component of the output wave collapse into a brilliant centre (not shown here). But the output right circular component beam collapses into a narrow brilliant ring with a much weaker diameter:  $31 \mu\text{m}$  (Fig. 3 (c1) experimental and 3 (c2) theoretical). A similar description than in the ring plane can be performed: interference pattern with the reference beam (Fig. 3 (d1)) and calculated phase (Fig. 3 (d2)) with an optical vortex in the centre.

### 4.3 Configuration generating a fractional angular orbital momentum

Generally speaking the CR of an elliptical polarized beam leads to an output beam, after projection on another elliptical state, with a fractional OAM. In this subsection we launch a left-circular polarization beam through the BZBO sample and we project the output beam on a linear polarized state with  $-45^\circ$  angle from the horizontal axis. The intensity in the focal plane is represented in Fig. 4 (a1) (experimental) and 4 (a2) (theoretical). The light is localised on the upper semi-circle with the presence of the dark ring. The phase of the wave is studied from the interference pattern with the reference beam (Fig. 4 (b1)). Following a closed path inside the dark ring as the one visualised by the green ellipse, and counting the number of brilliant fringes, we find that the phase variation is 0 along this round trip. This is confirmed by following the same path on the theoretical Fig. 4 (b2). To the contrary, following a closed path outside the dark ring as the red circle in Fig. 4 (b1), we find that there is one surplus fringe in the lower semi-circle corresponding to  $2\pi$  phase variation on a round trip. This is confirmed by following a similar phase trip in the theoretical Fig. 4 (b2).

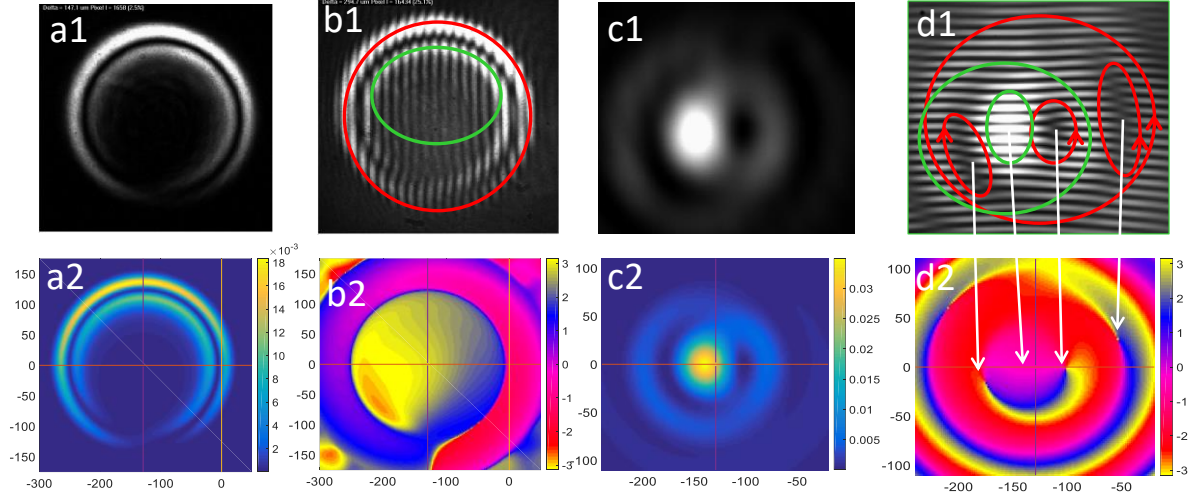


Fig. 4 See text in subsection 4.3. Columns a and b: focal plane, columns c and d: Raman spot plane. Columns a and c: near field intensity; column b and d: 1: interference with the reference beam and phase (vertical scale in rad.). Line 1: experimental, lines 2: theoretical.

The OAM calculated with Eq. (10) is found to be  $0.456 \hbar/\text{photon}$  (and the SAM is  $0 \hbar/\text{photon}$  because the polarization is linear).

In the plane about 2 cm further (the Raman spot plane) the beam intensity distribution is modified and we can see a brilliant area surrounded by dark ones: Fig. 4 (c1) (experimental) and 4 (c2) (theoretical). The experimental interference pattern with the reference beam is visualized in Fig. 4 (d1). We have drawn three small red ellipses. Each of them surrounds a field of fringes such that there is a surplus brilliant one either in the left part of the ellipse either in the right part. In the first case (one ellipse) the meaning is  $2\pi$  phase variation in the clock-wise round trip and in the second case (two ellipses)  $2\pi$  phase variation in the anticlock-wise round trip. We have drawn a small green ellipse surrounding an area with no surplus brilliant fringe, meaning no phase variation following a round trip. Three white arrows have been added to link the centres of the three red ellipses with the three optical vortices found in the theoretical description of the phase represented in Fig. 4 (d2). A fourth white arrow has been drawn to link the centre of the green circle to the area calculated to be regular. A full agreement is observed between the calculated phase variation and the interference pattern. A large green circle is also drawn in Fig. 4 (d1) with no surplus brilliant fringe following a round trip. This is explained because it surrounds one clockwise and one anticlock-wise  $2\pi$  phase variation areas. A large red circle is drawn with one surplus brilliant fringe following a round trip. This is explained because it surrounds one clockwise and two anticlock-wise  $2\pi$

phase variation areas. Once more these phase variations can be found also following similar paths in the theoretical Fig. 4 (d2).

## 5. Conclusion

We have grown an acentric biaxial BZBO single crystal by the Kyropoulos method under conditions of low temperature gradients. It was oriented and cut perpendicular to the optical axis located in the *ab* plane at  $42.6^\circ$  from the *a*-axis. We focused slightly behind the sample the Gaussian beam from a He-Ne laser at 632.8 nm and we made magnified images of the near field on a CCD camera. Linear polarizers and quarter-wave plates were used to launch and detect beams with various circular, elliptic or linear polarization states. A reference beam was taken from the entrance and redirected on the CCD screen to obtain a controlled wedge fringe pattern visualising the phase of the wave. The specific rotatory power was measured to be 2.74 rad/cm. We present results of conoscopy patterns obtained launching through the crystal slab a left-circular polarized beam and projecting the output beam on a right-circular polarization state or on a linearly polarization state at  $-45^\circ$  from the horizontal axis. All the experimental results (optical activity, intensity and phase of the output wave and vortices) are well described by a theoretical model based on the bi-anisotropy of the BZBO crystal. The OAM and SAM are calculated for each configuration from the distribution of the transverse electric field.

## References

1. Feng Li, Shilie Pan, Xueling Hou, and Jun Yao, “A Novel Nonlinear Optical Crystal  $\text{Bi}_2\text{ZnOB}_2\text{O}_6$ ”, *Cryst. Growth & Design*, **9**, 4091-4061 (2009).
2. Feng Li, Xueling Hou, Shilie Pan, and Xian Wang, “Growth, Structure, and Optical Properties of a Congruent Melting Oxyborate,  $\text{Bi}_2\text{ZnOB}_2\text{O}_6$ ”, *Chem. Mater.* **21**, 2846–2850 (2009).
3. A. Brenier, A. Majchrowski, E. Michalski “Chirality versus dichroism: competition and role in conical diffraction displayed from the  $\text{Nd}:\text{Bi}_2\text{ZnOB}_2\text{O}_6$  acentric biaxial laser crystal”, *Optical Materials* **72**, 813-820 (2017).
4. C. Chen, “Development of new nonlinear optical crystals in the borate series”, *Laser Science and Technical International Handbook*, Vol. 15, Harwood, New York, 1993.

5. T. Sasaki, Y. Mori, M. Yoshimura, Y. Khin Yap, T. Kamimura, “Recent development of nonlinear optical borate crystals: key materials for generation of visible and UV light”, *Mat. Sci. and Eng.*, **30**, 1-54 (2000).
6. “Structure-Properties relationship in Non-Linear Optical Crystals I”, Volume Editors: Xin-Tao Wu, Ling Chen, vol. 144, 2012, Structure and bonding, Series Editors D. M. P. Mingos, Springer.
7. M. J. Padgett, “Orbital angular momentum 25 years on”, *Opt. Exp.*, **25** (10), 11265-11274 (2017).
8. M. W. Beijersbergen, R. P. C. Coerwinkel, M. Kristensen, and J. P. Woerdman, “Helical-wavefront laser beams produced with a spiral phaseplate,” *Opt. Commun.* **112** (5-6), 321–327 (1994).
9. A. Jesacher, A. Schwaighofer, S. Fürhapter, C. Maurer, S. Bernet, and M. Ritsch-Marte, “Wavefront correction of spatial light modulators using an optical vortex image,” *Opt. Exp.*, **15** (9), 5801–5808 (2007).
10. L. Allen, M. W. Beijersbergen, R. J. C. Spreeuw, and J. P. Woerdman, “Orbital angular momentum of light and the transformation of Laguerre-Gaussian laser modes”, *Phys. Rev. A*, **45** (11), 8885-8889, 1992.
11. L. Landau and E. Lifchitz, *Electrodynamique des milieux continus*, Ed. Mir Moscou 1969.
12. M. Born, E. Wolf, A. B. Bhatia, *Principles of optics: electromagnetic theory of propagation, interference and diffraction of light*, 7<sup>th</sup> ed. Cambridge University Press, 1999.
13. A. Turpin, Y. V. Loiko, T. K. Kalkandjiev, and J. Mompart, “Conical refraction: fundamentals and applications”, *Laser Photonics Rev.*, 1–22 (2016).
14. D. P. O’Dwyer, C. F. Phelan, K. E. Ballantine, Y. P. Rakovich, J. G. Lunney, and J. F. Donegan, “Conical diffraction of linearly polarized light controls the angular position of a microscopic object”, *Opt. Express* **18** (26), 27319-27326 (2010).
15. M. V. Berry, M. R. Jeffrey, and M. Mansuripur, “Orbital and spin angular momentum in conical diffraction”, *J. opt. A: pure Appl. Opt.* **7**, 685-690 (2005).
16. D. P. O’Dwyer, C. F. Phelan, Y. P. Rakovich, P. R. Eastham, J. G. Lunney, and J. F. Donegan, “Generation of continuously tunable fractional optical angular momentum using internal conical diffraction”, *Opt. Express*, **18** (16), 16480-16485 (2010).
17. A. Brenier, “Lasing with conical diffraction feature in the KGd(WO<sub>4</sub>)<sub>2</sub>:Nd biaxial crystal”, *Appl. Phys. B: Las. and Opt.* 122:237 (2016).



18. Jin Au Kong, *Electromagnetic wave theory*, EWMH publishing, Cambridge, Massachusetts, USA.
19. M. V. Berry, “The optical singularities of bianisotropic crystals”, *Proc. R. Soc. A*, **461**, 2071-2098 (2005).

### Figure captions

1. Experimental set-up for CR and OAM visualisation.
2. column a: intensity of the far field; column b: intensity of the near field in the focal plane; column c: 1 and 3 interference with the reference beam, 2 and 4 phase in the focal plane (vertical scale in rad.). Lines 1 and 3: experimental, lines 2 and 4: theoretical.
3. See text in subsection 4.2. Columns a and b: focal plane, columns c and d: Raman spot plane. Columns a and c: near field intensity; column b and d: 1: interference with the reference beam and phase (vertical scale in rad.). Line 1: experimental, lines 2: theoretical.
4. See text in subsection 4.3. Columns a and b: focal plane, columns c and d: Raman spot plane. Columns a and c: near field intensity; column b and d: 1: interference with the reference beam and phase (vertical scale in rad.). Line 1: experimental, lines 2: theoretical.